JOURNAL OF PROPULSION AND POWER
Vol. 17, No. 2, March–April 2001

Analysis and Design of the Inductor-Current-Sensing Peak-Power-Tracking Solar-Array Regulator

Yoon-Jay Cho* and Bo-Hyung Cho†
Seoul National University, Seoul, Korea 151-742

An analysis and design of a peak-power-tracking solar-array regulator that senses the inductor current are proposed. Because it uses the inductor current as the solar-array output-power information, the peak-power-tracking control scheme can be greatly simplified. The charge-controlled two-loop scheme is presented to improve the undesired dynamics caused by the interaction between the inductor current and the peak-power-tracking loop. The comparison between the single-voltage-loop-controlled system and the two-loop-controlled system that uses the charge control is presented.

Nomenclature

Constants

C	=	capacitor value of the solar-array regulator, F
C_f	=	capacitor value of the filter stage in the solar-array regulator, F
C_t	=	capacitor value in switch current-sensing network, F
D	=	duty ratio of the solar-array regulator
F_{sw}	=	switching frequency of the solar-array regulator, Hz
L	=	inductor value of the solar-array regulator, H
L_f	=	inductor value of the filter stage in the solar-array regulator, H
Rc	=	parastic resistance of the capacitor, Ω
Rl	=	parastic resistance of the inductor, Ω
r_S	=	dynamic resistance of the solar array, Ω
T_S	=	sampling peroid of the peak-power-tracking controller, s
ω_S	=	sampling frequency of the peak-power-tracking controller, rad/s

Variables

I_L	=	inductor current of the solar-array regulator, A
I_S	=	solar-array output current, A
I_{SW}	=	switch current in the solar-array regulator, A
P_S	=	solar-array output power, W
V_{bat}	=	battery voltage, V
V_C	=	control voltage of the inner loop, V
V_{ref}	=	reference voltage of the solar array generated by the peak-power-tracking controller, V
V_S	=	solar-array output voltage, V
V_t	=	voltage of the current-sensing transfomer, V
$\hat{x}$	=	small-signal disturbance of variable X

Transfer Functions

Fm	=	pulse-width-modulation (PWM) gain of the inner loop
Gvd	=	transfer function from the duty ratio to the solar-array voltage
Gid	=	transfer function from the duty ratio to the inductor current
Hv	=	transfer function of the inner voltage loop
Hi	=	transfer function of the inner current loop
PPT	=	transfer function of the peak-power-tracking controller
Tv	=	$FmHvGvd$
Ti	=	$FmHiGid$

Received 31 January 2000; revision received 10 April 2000; accepted for publication 20 June 2000.

*Ph. D. Candidate, Power Electronics System Laboratory, School of Electrical Engineering, #043 SOEE, Kwan-Ak P.O. Box 34; feelso@snu.ac.kr. Member AIAA.

†Professor, Power Electronics System Laboratory, School of Electrical Engineering, #043 SOEE, Kwan-Ak P.O. Box 34; bhcho@snu.ac.kr.

I. Introduction

FOR a low-Earth-orbit (LEO) spacecraft power system, a solar-array regulator (SAR) processes the solar-array power to charge the battery and to supply the load power during the sunlight period. The SAR operates mainly in two modes: the peak-power-tracking (PPT) mode and the current-regulation (CR) mode, depending on the status of the battery and the load-power demand.[1,2] As shown in Fig. 1, the output characteristic of the solar array is highly nonlinear and its output power depends on the operating point, which is set by the SAR. The peak-power point varies with the temperature, the illumination level, and the age of the solar array. Especially for a LEO spacecraft power system, which has short orbit cycles and undergoes wide temperature and illumination variations, it is necessary to have adaptive tracking capability for this peak-power point. Figure 2 illustrates a series SAR system widely used in a LEO spacecraft power system in the PPT mode. The inner voltage loop regulates the solar-array output voltage to the reference value from the PPT controller. The PPT controller calculates the solar-array power slope by multiplying the sensed solar-array voltage and current. If this power slope is positive, the PPT controller increases the reference value until the sensed power slope is negative, and vice versa. By this method, the operating point of the solar array is located near the peak-power point, where the power slope is zero. This algorithm can be expressed as

$$V_{ref}(k+1) = V_{ref}(k) + M\frac{\Delta P_S}{\Delta V_S} \tag{1}$$

where M is the gain of the PPT controller that uses the power-sensing scheme.

As shown in Fig. 2, for a given battery voltage, the average value of the inductor current is proportional to the solar-array power. A simple PPT scheme in which only the inductor current I_L in the SAR is sensed for the PPT algorithm is presented in Fig. 3 (Ref. 3, 4). This system greatly simplifies the PPT scheme, especially for an analog PPT scheme, because the multiplying operation in the PPT controller is not necessary. The conventional algorithm in Eq. (1) can be used in this system as

$$V_{ref}(k+1) = V_{ref}(k) + Mi\frac{\Delta I_L}{\Delta V_S} \tag{2}$$

where Mi is the gain of the PPT controller that uses the inductor-current-sensing scheme. For the same dc gain of the power-sensing scheme, Mi must be set to MV_{bat}.

Even though the steady-state value of the inductor current is proportional to the solar-array output power, their dynamic responses

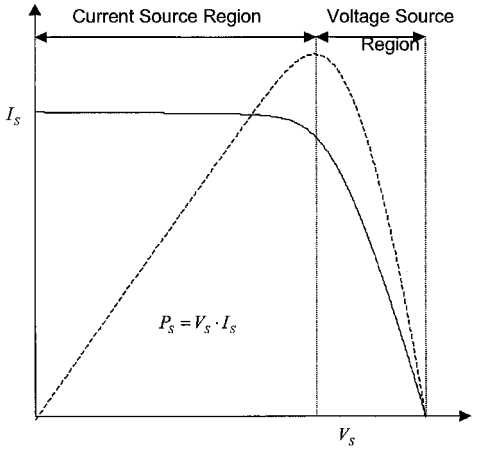

Fig. 1 Characterisitc curve of the solar array.

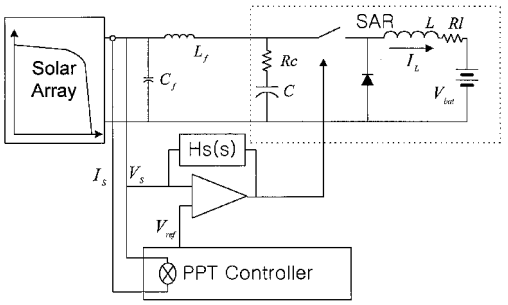

Fig. 2 Conventional power-sensing PPT system.

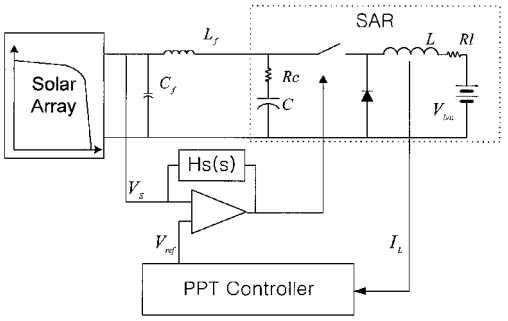

Fig. 3 Inductor-current-sensing system.

and hence the stability conditions are quite different. As the solar-array output characteristic changes, this directly reflects the solar-array output-power sensing scheme in the system in Fig. 2, whereas this perturbation information appears in the inductor current after going through the converter dynamics in the system in Fig. 3. This has detrimental effects on the PPT control loop and possibly causes stability problems. The simulation result in Fig. 4, in which the same effective controller gain and sampling frequency as those in Fig. 3 are used, shows unstable operation in the inductor-current-sensing scheme. To overcome these undesired dynamic interactions, a multiple-loop current-mode control can be used.

In Sec. II, a small-signal analysis of the single-loop- (voltage-loop-) controlled inductor-current-sensing system is performed to analyze the interaction of the inductor-current dynamics with the PPT loop. In Sec. III, an analysis and design of the charge-controlled current-mode system are presented, and performance verification through computer simulation is also presented. Also, the problems and the difficulties with peak-current-mode control are discussed.

II. Small-Signal Analysis of a Single-Loop-Controlled System

Figure 5 shows the control block diagram of the power-sensing PPT system. $G(s)$ is the transfer function of the SAR from the reference voltage to the solar-array output voltage, $\hat{V}_S/\hat{V}_{\text{ref}}$, and $F(s)$

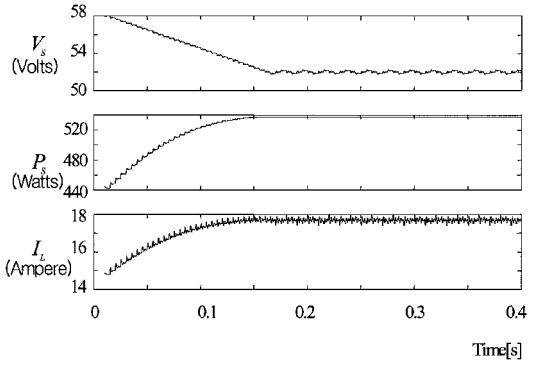

a) Power-sensing scheme

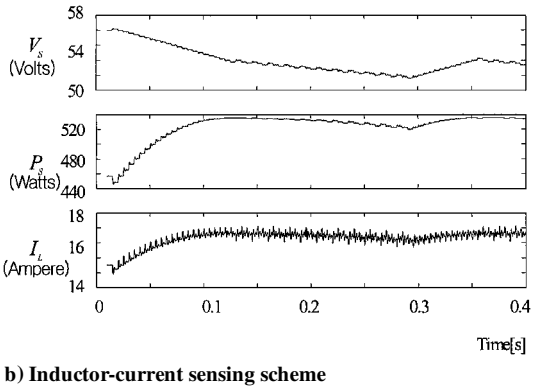

b) Inductor-current sensing scheme

Fig. 4 Simulation results.

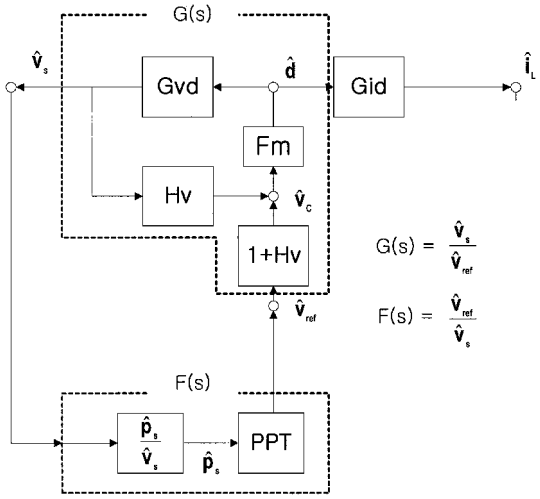

Fig. 5 Control block diagram of the power-sensing scheme.

is the transfer function of the PPT controller from the solar-array voltage to the reference voltage, $\hat{V}_{\text{ref}}/\hat{V}_S$. Integration of these two blocks causes a feedback network system. Thus, in this system, the stability of the PPT loop depends on the overall loop gain (T_d) as in

$$T_d = [G(s)][F(s)] \tag{3}$$

This shows that the stability of the power-sensing scheme depends on the dynamics of the solar-array voltage. The transfer function from the solar-array voltage to the reference voltage in Eq. (3) can be derived as Eq. (4) from the small-signal analysis of Eq. (1), with the zero-order-hold effect in discrete characteristics in the PPT controller:

$$\frac{\hat{v}_{\text{ref}}}{\hat{v}_S} = \frac{MI_P}{V_P}\frac{1}{s}\frac{e^{sT_S}+1}{e^{2sT_S}} \tag{4}$$

where I_P is the current of the solar array and V_P is the voltage of the solar array when the operating point is located near the peak-power point.

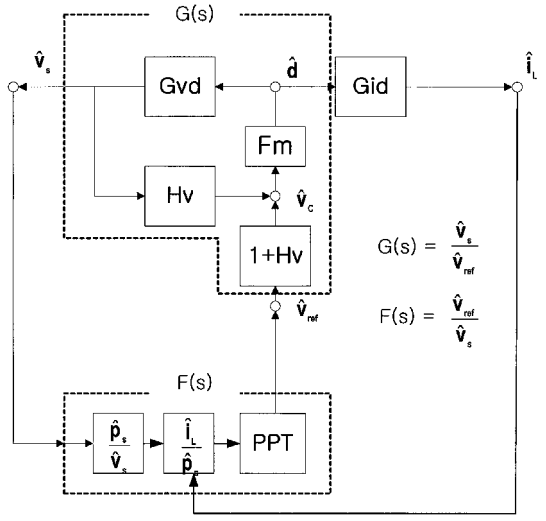

Fig. 6 Control block diagram of the inductor-current-sensing scheme.

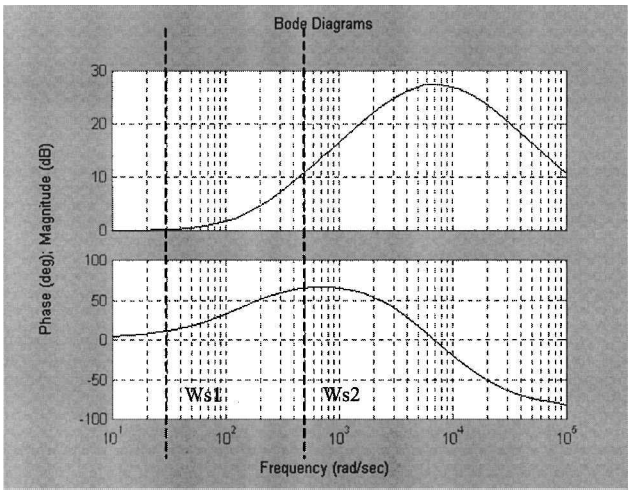

Fig. 7 Bode plot of the inductor dynamics $[V_{bat}(\hat{i}_L/\hat{p}_S)(\omega)]$.

In the inductor-current-sensing scheme in Fig. 6, the sensed inductor-current information in Eq. (2) can be divided into the two factors as in Eq. (5). The first factor $(\Delta P_S/\Delta V_S)$ represents the solar-array output-power slope with respect to the solar-array voltage variation, and the second factor $(\Delta I_L/\Delta P_S)$ is the inductor-current dynamics in this system:

$$\frac{\Delta I_L}{\Delta V_S} = \frac{\Delta P_S}{\Delta V_S}\frac{\Delta I_L}{\Delta P_S} \tag{5}$$

Because these two terms are functions of time, as expressed in Eq. (1), the transfer function in the frequency domain is difficult to derive. However, if the power variation is assumed to be the sinusoidal function with constant frequency (sampling frequency of the PPT controller), the inductor-current dynamics can be expressed as a complex constant, and Eq. (5) can be expressed as Eq. (6). A detailed derivation is included in the Appendix.

$$\frac{\Delta I_L}{\Delta V_S} = \frac{\Delta P_S}{\Delta V_S}\frac{\hat{I}_L}{\hat{P}_S}(\omega)\bigg|_{@\omega=\varpi_S} \tag{6}$$

$$\frac{\hat{i}_S}{\hat{p}_S}(\omega) = \frac{1}{Ik}\frac{HvFmGid}{1+Tv} \tag{7}$$

Figure 7 is the Bode plot of the transfer characteristic from the solar-array output power to the inductor current [Eq. (7)], which shows that the effect of the inductor-current dynamics is unity without any phase delay where the sampling frequency is sufficiently low.

However, as the sampling frequency increases, the gain and the phase distortion that are due to the inductor dynamics become pronounced. Furthermore, the peaking frequency of the inductor dynamics moves to the lower-frequency region as the operating point of the solar array moves to the peak-power point.

To avoid the detrimental effect of the inductor dynamics, the sampling frequency must be limited to the low frequency or a low-pass filter must be added to the feedback loop. However, the cutoff frequency of the low-pass filter must be low. This delays the speed of the overall feedback loop and makes the dynamic performance of the system poor.

III. Current-Mode Control

Instead of using an additional low-pass filter or limiting the speed of the PPT controller, the current-mode control is proposed. Because the inductor-current information is fed back and incorporated to determine the duty ratio of the SAR, this additional current loop should be able to improve the system dynamics. From Fig. 8, the inductor dynamics with the current loop closed becomes

$$\frac{\hat{i}_S}{\hat{p}_S}(\omega) = \frac{1}{Ik}\frac{HvFmGid}{1+Tv+Ti} \tag{8}$$

$$= \frac{1}{Ik}\frac{(Hv/Hi)Ti}{1+Tv+Ti} \approx \frac{1}{Ik}\frac{Hv}{Hi} \tag{9}$$

when $Ti \gg 1+Tv$.

From Eq. (8), it can be seen that if the current loop (Ti) dominates over the voltage loop gain (Tv), the inductor-current dynamics (Gid) cancels out as Eq. (9), especially in the frequency range where the inductor dynamics become interactive—region B in Fig. 9. Figure 9 shows the relative magnitude of Ti and Tv for a properly designed

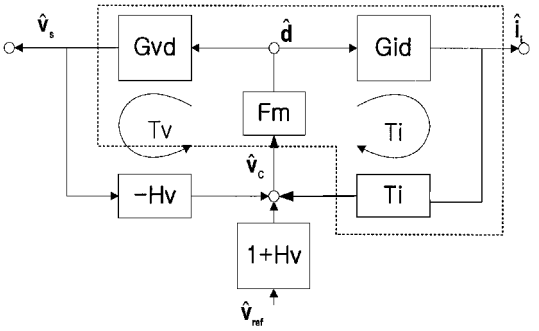

a) Control block diagram

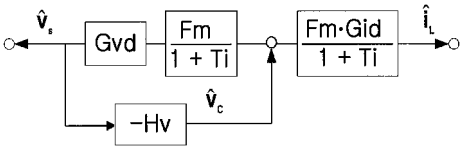

b) Simplified control block diagram

Fig. 8 Control block diagram of the two-loop-controlled system.

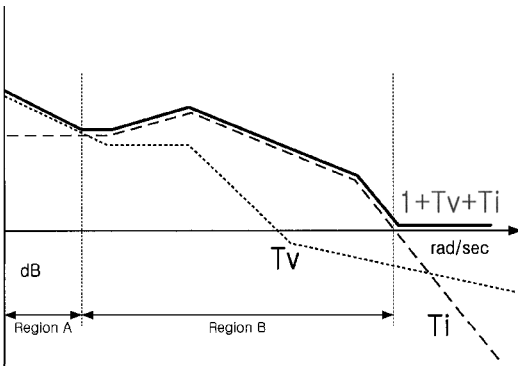

Fig. 9 Effect of the current loop.

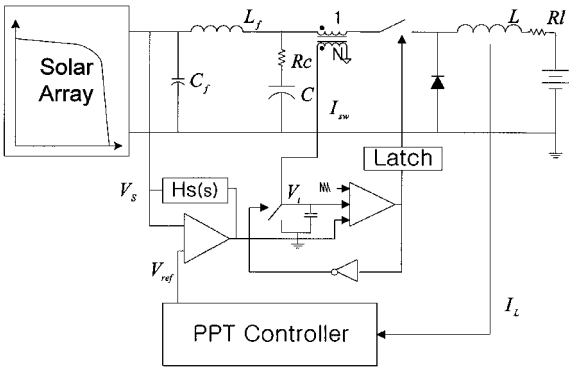

Fig. 10 Charge-control scheme.

system. Furthermore, the current-mode control offers inherent current protection without additional circuits.

Charge-Current-Mode Control

Among various current-mode controls, the charge-current-mode (CCM) control scheme in Fig. 10 is proposed.[5–7] The peak-current mode (PCM) or the average-inductor-current mode (ACM) cannot be used because the dynamics of the current loop is quite different between the operating point in the current-source region and the voltage-source region of the solar-array output. This is because, as shown in Fig. 1, the inductor-current gain function with respect to the solar-array voltage changes its sign as the operating point moves from the current-source region to the voltage-source region. In fact, PCM or ACM control results in a nonminimum phase system.

In Fig. 10 the capacitor in the current-sensing network integrates the switch current to obtain the charge information of the switch current per cycle. The voltage loop regulates the solar-array output voltage by controlling this charger current. In this scheme the following condition is satisfied in each switching cycle:

$$V_t = \frac{1}{C_t}\int_0^{dT_{sw}} I_L(t)\,dt = \frac{T_{sw}}{C_t}\bar{i}_{sw} \tag{10}$$

where T_{sw} is the switching period and $\bar{i}_{sw}$ is the average switch current.

The time average value of the switch current has the same dynamic information as the solar-array current in this system. Thus the solar-array current information is fed back and incorporated to control the solar-array voltage.

External Ramp Design

The charge control has an inherent instability problem as in the peak-current-mode control when the duty ratio is over 50%. This subharmonic oscillation occurs when the following condition is not satisfied[5–7]:

$$I_{LPK} > S_f T_{sw}/2 \tag{11}$$

where I_{LPK} is the inductor peak current and S_f is the falling slope of the charge-current waveform.

This condition may not be satisfied in this power stage when the solar-array power is low. To avoid this inherent subharmonic oscillation, an external ramp must be added. The stability condition with the external ramp is

$$\frac{LF_{sw}I_{LPK}}{V_{bat}} + \frac{LF_{sw}C_t'Se}{V_{bat}} - \frac{1}{2} > 0 \tag{12}$$

where $C_t' = NC_t$, N is the turn ratio of the current-sensing transformer in Fig. 10, and Se is the external ramp slope.

To make the current loop stable in the entire operating range, the external ramp slope (Se) is designed to meet this condition even if I_{LPK} is zero in condition (12).

Voltage-Loop Design

In designing the voltage loop, the switching regulator with the current loop closed can be treated as a new power stage—the block with a dotted line in Fig. 8. Then the effective loop gain (defined at point A in Fig. 8) becomes the product of the control to the output transfer function ($\hat{v}_S/\hat{v}_C$) of the new power stage [Eq. (13)] and the loop compensation function. Thus, based on the transfer function in Eq. (13), the compensator can be designed:

$$\left.\frac{\hat{v}_S}{\hat{v}_C}\right|_{@Ti\,\text{closed}} = Gi\,\frac{(1+s/\omega_{Z1})(1+s/\omega_{Z2})}{(1+s/\omega_v)\left(1+s/Q_P\omega_n+s^2/\omega_n^2\right)} \tag{13}$$

A detailed expression of the constant in Eq. (13) is included in the Appendix. The 2 pole—1 zero compensator is used in this voltage controller.

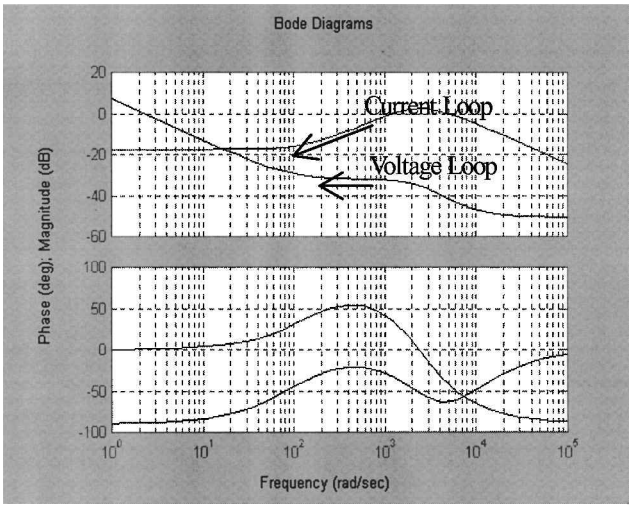

Fig. 11 Current (Ti) and voltage gain (Tv) in the charge control.

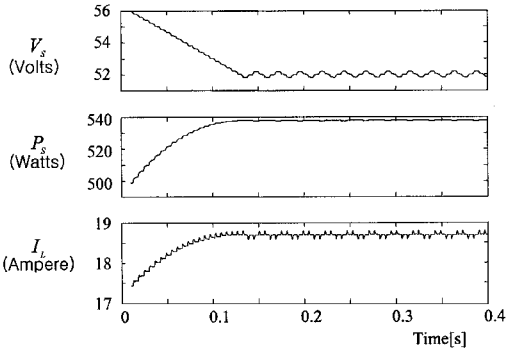

Fig. 12 Simulation results (charge-control scheme).

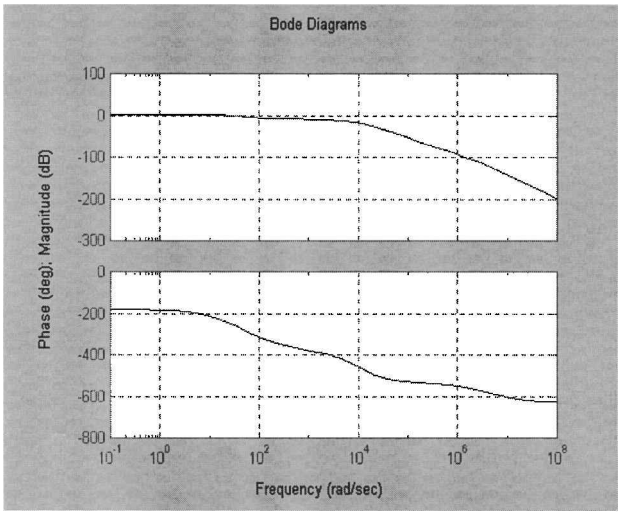

Fig. 13 Bode plot of the inductor dynamics [$V_{bat}(\hat{i}_L/\hat{p}_S)(\omega)$].

Figure 11 shows Ti and Tv when the operating point of the solar array is near the peak-power point. Figure 12 shares the simulation results of the proposed system that uses the charge control. The same conditions as in the case of Fig. 4 are applied to this simulation, but in this case, the results show a stable operation because the inductor dynamics is improved as in Fig. 13 (compare with Fig. 7).

IV. Conclusion

The inductor-current-sensing system can greatly simplify the PPT controller because it does not need a multiplying operation. Dynamic interaction between the inductor current and the PPT loop is analyzed, and it shows that the interaction causes detrimental effects and possibly a stability problem in the PPT system. A multiloop control that uses the current-mode control effectively solves the problem. Among various current-mode controls, the CCM control is implemented. It is shown that the PCM control cannot be used for this scheme. Simulation results show the effectiveness of the proposed control scheme.

Appendix

Derivation of Eq. (6)

$$\Delta I_L(t) = \int_{-\infty}^{\infty} \frac{\hat{i}_L}{\hat{p}_S}(\omega)\Delta P(j\omega)e^{j\omega t}\,\mathrm{d}\omega$$

Assume that $\Delta P(j\omega) = \Delta P\sigma(\omega - \omega_S)$, where $\sigma(\omega)$ is the impulse function,

$$= \int_{-\infty}^{\infty} \frac{\hat{i}_L}{\hat{p}_S}(\omega)\Delta P\sigma(\omega - \omega_S)e^{j\omega t}\,\mathrm{d}\omega$$

$$= \frac{\hat{i}_L}{\hat{p}_S}(\omega_S)\Delta P e^{j\omega_S t}$$

[Eq. (8)], where

$$Gid = \frac{Ik}{D^2}\frac{[s(V_S C/Ik) + 1]}{\Delta(s)}$$

where

$$Ik = (V_S/r_S - I_S)$$

$$Gvd = \left(V_{\text{bat}}/D^2\right)(\{[s(I_L L/V_{\text{bat}}) + 1](sRcC + 1)\}/\Delta(s))$$

$$\Delta(s) = s^2/LC + s\left[(Rc + Rl/D^2)C - 1\Big/D^2 r_S\right] + 1$$

Constants of Condition (11)

$$\omega_{Z1} = \frac{1}{RcC}, \qquad \omega_{Z2} = \frac{DV_{\text{bat}}}{I_S L}, \qquad \omega_n = \frac{\pi}{T_{\text{sw}}}$$

$$Fm = \frac{C_t}{(I_{LP} + SeC_t)T_{\text{sw}}}, \qquad Ri = \frac{D}{C_t F_{\text{sw}}}$$

$$Q_P = 1\Big/\pi\left(\frac{LF_{\text{sw}}I_L}{V_{\text{bat}}} - \frac{D}{2} + \frac{LF_{\text{sw}}C_t Se}{V_{\text{bat}}}\right)$$

$$Gi = \frac{Fm\left(V_{\text{bat}}\Big/D^2\right)}{1 + KfFm\left(V_{\text{bat}}\Big/D^2\right) + RiFm(Ik/D^2)}$$

where

$$Ik = (V_S/r_S - I_S)$$

$$\omega_V = \frac{1 + KfFm\left(V_{\text{bat}}\Big/D^2\right) + RiFm(Ik/D^2)}{(Rc + Rl/D^2)C - 1\Big/D^2 r_S + KfFm(V_{\text{bat}}\Big/D^2)[(\omega_{Z1} + \omega_{Z2})/\omega_{Z1}\omega_{Z2}] + RiFm(Ik/D^2)(r_S C - T_S/2)}$$

$$\Delta P_s(t) = \int_{-\infty}^{\infty} \Delta P_S(j\omega)e^{j\omega t}\,\mathrm{d}\omega = \Delta P e^{j\omega_S t}$$

Thus

$$\frac{\Delta I_L}{\Delta P_S} \approx \left[\frac{\hat{i}_L}{\hat{p}_S}(\omega)\right]\Bigg|_{@\omega = \varpi_S}$$

Derivation of Eqs. (7) and (8)

$$\hat{p}_S = -(V_S/r_S - I_S)\hat{v}_S \triangleq -Ik\hat{v}_S, \qquad \hat{i}_S/\hat{p}_S = -(1/Ik)(\hat{i}_S/\hat{v}_S)$$

Without the current loop ($Ti = 0$) and from Fig. 8b,

$$\frac{\hat{i}_S}{\hat{p}_S} = \frac{1}{Ik}\frac{HvFmGid}{1 + Tv}$$

[Eq. (7)]. With the current loop (Ti) and from Fig. 8b,

$$\frac{\hat{i}_S}{\hat{p}_S} = \frac{1}{Ik}\frac{HvFmGid}{1 + Tv + Ti}$$

References

[1] Huynh, P., and Cho, B. H., "Analysis and Design of a Microprocessor-Controlled Peak-Power Tracking System," *Proceedings of the Intersociety Energy Conversion Engineering Conference*, American Nuclear Society, Illinois, 1992, pp. 1.63–1.78.

[2] Kim, S. J., and Cho, B. H., "Analysis of Spacecraft Battery Charger Systems," *Proceedings of the Intersociety Energy Conversion Engineering Conference*, Society of Automotive Engineers, Warrendale, PA, 1990, pp. 365–372.

[3] Caldwell, D. J., Bavaro, L. T., and Carian, P. J., "Advanced Space Power System with Optimized Peak Power Tracking," *Proceedings of the Intersociety Energy Conversion Engineering Conference*, American Institute of Chemical Engineers, New York, 1991, pp. 145–150.

[4] Cho, B. H., and Lee, F. C., "Large Signal Analysis of Spacecraft Power Systems," *IEEE Transactions on Power Electronics*, Vol. 5, No. 1, 1990, pp. 110–115.

[5] Ridley, R. B., "A New, Continuous-Time Model for Current Mode Control," *IEEE Transactions on Power Electronics*, Vol. 6, No. 2, 1991, pp. 271–280.

[6] Tang, W., Lee, F. C., Ridley, R. B., and Cohen, I., "Charge Control: Modeling, Analysis and Design," *IEEE Proceedings of Power Electronics Specialists' Conference*, Inst. of Electrical and Electronics Engineers, New York, 1992, pp. 503–511.

[7] Voperian, V., "The Charge-Controlled PWM switch," *IEEE Proceedings of Power Electronics Specialists' Conference*, Inst. of Electrical and Electronics Engineers, New York, 1996, pp. 533–542.